

Direct Conversion X-Ray Detectors with High Sensitivity at Low Dose Rate Based on All-Inorganic Lead-Free Perovskite Wafers

Cuixian Zhang

Chengdu University of Information and Technology, Chengdu, China
Email: 945757071@qq.com

How to cite this paper: Zhang, C.X. (2022) Direct Conversion X-Ray Detectors with High Sensitivity at Low Dose Rate Based on All-Inorganic Lead-Free Perovskite Wafers. *Detection*, 9, 13-27.
<https://doi.org/10.4236/detection.2022.92002>

Received: March 6, 2022

Accepted: April 27, 2022

Published: April 30, 2022

Copyright © 2022 by author(s) and Scientific Research Publishing Inc.
This work is licensed under the Creative Commons Attribution International License (CC BY 4.0).
<http://creativecommons.org/licenses/by/4.0/>



Open Access

Abstract

Just as lead-based perovskites that are hot in solar cell preparation, Bi-based perovskites have demonstrated excellent performance in direct X-ray detection, especially the $\text{Cs}_3\text{Bi}_2\text{I}_9$ single crystals (SCs). However, compared with lead-halide perovskites, one challenge for the $\text{Cs}_3\text{Bi}_2\text{I}_9$ SCs for X-ray detection application is that it is difficult to prepare large-sized and high-quality SCs. Therefore, how to get a large area with a high-quality wafer is also as important as $\text{Cs}_3\text{Bi}_2\text{I}_9$ growth method research. Here, different anti-solvents are used for the preparation of poly-crystalline powder with the Antisolvents precipitation (A) method, as a control, High-energy ball milling (B) was also used to prepare poly-crystalline powders. The resultant two types of $\text{Cs}_3\text{Bi}_2\text{I}_9$ wafer exhibit a micro-strain of 1.21×10^{-3} , a resistivity of $5.13 \times 10^8 \Omega \text{ cm}$ and a microstrain of 1.21×10^{-3} , a resistivity of $2.21 \times 10^9 \Omega \text{ cm}$. As a result, an X-ray detector based on the high-quality $\text{Cs}_3\text{Bi}_2\text{I}_9$ wafer exhibits excellent dose rate linearity, a sensitivity of $588 \mu\text{C} \cdot \text{Gy}_{\text{air}}^{-1} \cdot \text{cm}^{-2}$ and a limit of detection (LoD) of $76 \text{ nGy}_{\text{air}} \cdot \text{s}^{-1}$.

Keywords

X-Ray Detection, Sensitivity, $\text{Cs}_3\text{Bi}_2\text{I}_9$

1. Introduction

In recent years, perovskite material (ABX_3), has been widely used in solar cell, visible light detection and Quantum dot luminescent material due to its high absorption coefficient, tunable bandgap and also has achieved a huge success in radiation detection [1]-[7].

In 2015, Yakunin *et al.* prepared a uniformly dense MAPbI_3 film by spin coating

or spraying on the substrate, prepared photodetectors based on the film, and successfully obtained X-ray images [8]. Since then, many researchers have joined in the application of perovskite materials in X-ray detection research, and have achieved very excellent results [9] [10] [11] [12]. But the existence of organic groups affects the stability of organic-inorganic hybrid perovskite materials. And the toxic of lead may cause environmental pollution, potential leakage and other dangers. Therefore, the research on inorganic lead-free perovskite materials is in full swing.

There are many lead-free perovskite materials, but $\text{Cs}_3\text{Bi}_2\text{I}_9$ is more suitable for X-ray detection because of its very similar structure to the Pb atomic shell structure and its large atomic mass. Bi-based lead-free perovskite materials, including $\text{MA}_3\text{Bi}_2\text{I}_9$, $\text{Cs}_3\text{Bi}_2\text{I}_9$, are outstanding in lead-free perovskite class.

In 2020, Zhang *et al.* grew centimeter-scale $\text{Cs}_3\text{Bi}_2\text{I}_9$ single crystals by high-temperature solution heating method and shape nucleus control. The sensitivity of the single crystal was as high as $1652.3 \mu\text{C}\cdot\text{Gy}^{-1}\cdot\text{cm}^{-2}$, and the detection limit was relatively low, reaching $130 \text{ nGy}\cdot\text{s}^{-1}$ [13]. Sun *et al.* prepared a 15 mm diameter $\text{Cs}_3\text{Bi}_2\text{I}_9$ single crystal by Briman hair [14]. The $\text{MA}_3\text{Bi}_2\text{I}_9$ single crystal sensitivity prepared by Liu *et al.* reached $872 \mu\text{C}\cdot\text{Gy}^{-1}\cdot\text{cm}^{-2}$ and the detection limit reached a very low $30 \text{ nGy}\cdot\text{s}^{-1}$ [15]. The above reports are based on photoconductive X-ray detectors based on perovskite materials. In recent years, some X-ray detectors are made of perovskite materials as new scintillator materials, which also have excellent performance [6] [16] [17] [18].

At present, there are many methods to prepare the photosensitive layer of X-ray detector in reported studies. The main methods currently used include spinning coating, scraping coating on the substrate to prepare polycrystalline thick film, melting method, solution method and other methods to grow perovskite single crystal and so on. However, spin coating method such as preparation of polycrystalline film thickness to meet the most X-ray materials of the best absorption thickness, and single crystal while performance is more outstanding, but its growth cycle taking a long time, the solution method of controllability and repeatability is poor, difficult to get the single crystal of large area. How to obtain high-quality large area to detect the cause of the core material? In this paper, piezoelectric ceramics and other experimental preparation methods were used to obtain the detector transport layer by pressing the polycrystalline powder obtained by the anti-solvent directly. In this paper, piezoelectric ceramics and other experimental preparation methods were used to obtain the detector transport layer by pressing the polycrystalline powder obtained by the anti-solvent directly.

2. Experimental

Preparation of $\text{Cs}_3\text{Bi}_2\text{I}_9$ Microcrystalline Powder: cesium iodide (CsI, 99.9%), bismuth triiodide (BiI_3 , 99.9%), N, N-dimethylformamide (DMF, 99.5%), dimethyl sulfoxide (DMSO, 99%) and Isopropyl alcohol (IPA, 99.5%) were purchased

from Aladin. All materials were used as received without further purification.

Two methods were employed to prepare $\text{Cs}_3\text{Bi}_2\text{I}_9$ polycrystalline powder, including A method and B method. In A case, CsI and BiI_3 with a mole ration of 3:2 was dissolved in DMF and DMSO component solvent (DMF:DMSO = 3:7). Immediately, the mixture was string at room temperature for 12 h. Add the clarified saturated solution filtered by $0.8\ \mu\text{m}$ PVDF filter into antisolvents isopropyl IPA, then centrifuge the orange turbid liquid, pull off the supernatant liquid, add appropriate amount IPA into centrifuge tube, then repeat the steps several times. Then, the sediment is vacuum-dried for 12 hours. As for B method, CsI and BiI_3 with same mole ration was mixed in the agate jar with agate balls, was milling for 8 h. The powders obtained by the above two methods will be used as pressing materials to get the photoelectric conversion layer.

Material Characterization: Crystallization characteristics and phase analysis were characterized by X-ray Diffractometer (XRD: TD-3500, HAO YUAN Instrument). The Optical properties were measured and characterized by UV-VIS spectrometer (UV-2550, Shimadzu). Thermal stability was characterized by Thermogravimetric Analysis instrument (STA 2500 Regulus, Shimadzu).

Fabrication of Devices: The polycrystalline powder obtained previously was pressed into shape at a pressure of 24 tons. The vertical $\text{Au}/\text{Cs}_3\text{Bi}_2\text{I}_9$ wafer/ Au devices were fabricated by depositing Au on two opposite surfaces of the slices, and the active area (electrode area) is $1 \times 8\ \text{mm}^2$. For resistivity and X-ray response investigate, 0.8 Pa, 4 min, $6\ \mu\text{A}$ was selected as the best deposition electrode process, Au electrode with thickness of 40 nm was obtained, the thickness of $\text{Cs}_3\text{Bi}_2\text{I}_9$ wafer-A and wafer-B are $666\ \mu\text{m}$ and $568\ \mu\text{m}$, respectively.

Device Characterization: The electrical properties and X-ray response of devices were characterized by Agilent (B2912A). A tungsten anode X-ray tube (Series 5000, Oxford Instruments) was used to perpendicularly irradiate devices. The dose rates were regulated by a gas ionization detector dosimeter system (ACCU-GOLD Touch AGD-P-AD, ACCU Digitizer AGDM+ and 10X6-3CT, Radcal). All equipment measurements are made under atmospheric ambient conditions and at room temperature. The test system is shown in **Figure 1**.

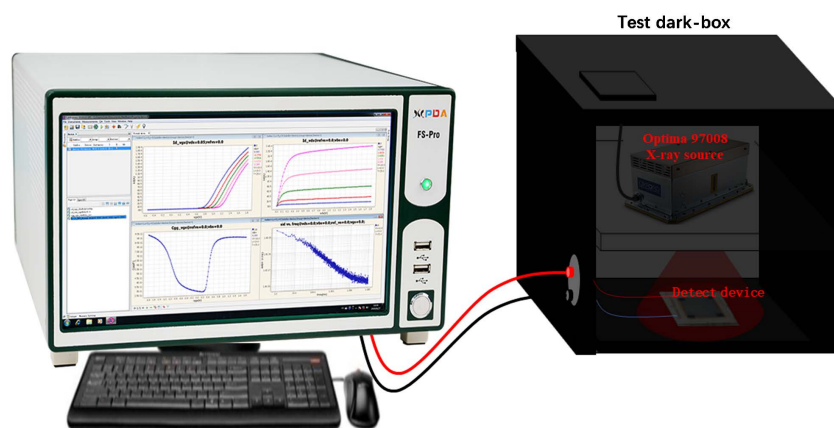


Figure 1. Schematic diagram of test system.

3. Result and Discussion

3.1. Characterizations of $\text{Cs}_3\text{Bi}_2\text{I}_9$

1) XRD

According to the current research, the photoelectric response of the device is closely related to the crystal quality of the materials. In order to obtain polycrystalline powder materials with excellent crystallization performance, the effects of different anti-solvents on crystallization performance of polycrystalline powder were investigated in the synthesis of polycrystalline powder by antisolvent method. Finally, we choose isopropanol as anti-solvents from ethanol, isopropanol, dichloromethane, n-hexane.

It is easy to find from the XRD pattern by horizontal comparison (**Figure 2**), the $\text{Cs}_3\text{Bi}_2\text{I}_9$ microcrystals synthesized by anti-solvent experiments have good crystallinity and are in good agreement with the standard PDF cards, as for $\text{Cs}_3\text{Bi}_2\text{I}_9$ powder prepared by ball milling method is shown in **Figure 2(b)**, the diffraction peak intensity is lower and the FWHM is large, indicating that the crystallinity is poor. The strongest diffraction intensity is lower than half of the worst strength of polycrystalline powder prepared by anti-solvent method. Vertical comparison, materials are obviously recrystallized after isostatic pressing treatment, the intensity of $\langle 006 \rangle$ in two wafer sample were stronger than powder, It can be said that $\langle 006 \rangle$ becomes the dominant crystal plane. Both ASP and HEBM dominant crystal faces, the $\{001\}$ crystallographic plane families' diffraction peaks of wafer are stronger than powder, meanwhile, the 100 crystallographic plane families' diffraction peaks are weaker, even the $\langle 110 \rangle$ was disappear. As we know $\text{Cs}_3\text{Bi}_2\text{I}_9$ is a hexagonal crystal system with the densest atoms and lowest energy along the C-axis, so the pressure recrystallizes the polycrystalline powder with energy. Therefore, the densest atoms provide the possibility of better X-ray absorption.

2) UV-VIS

The band gap of samples prepared by anti-solvent method is 2.24 eV. It is consistent with the theoretical and the calculated band gap of $\text{Cs}_3\text{Bi}_2\text{I}_9$ (2.30 eV) [19]. However, it is quite different from the actual reported band gap of $\text{Cs}_3\text{Bi}_2\text{I}_9$ single crystal material (1.96 eV [13] [20]). The possible reason is that the crystal grains are relatively small. According to the quantum domain effect, the smaller the crystal grains are, the more hypsochromic shift the absorption edge will be, and the band gap will be wider. The band gap width of the sample prepared by ball milling method is 2.3 eV, and the blue shift effect is more obvious.

As **Figure 3** shows, the absorption peaks of the samples were 484.6 nm and 487.2 nm respectively, which were basically around 485 nm. The reason for the absorption peaks was typical 0-dimensional $[\text{Bi}_2\text{I}_9]^{3-}$ bioctahedral quantum confinement effect, and the corresponding band width was about 2.55 eV [21], which proved that the band gap width of $\text{Cs}_3\text{Bi}_2\text{I}_9$ polycrystals obtained was also close to the theoretical value. At the same time, the transmittance shows that the $\text{Cs}_3\text{Bi}_2\text{I}_9$ absorbs the red light about 540 nm very obviously, which further confirms

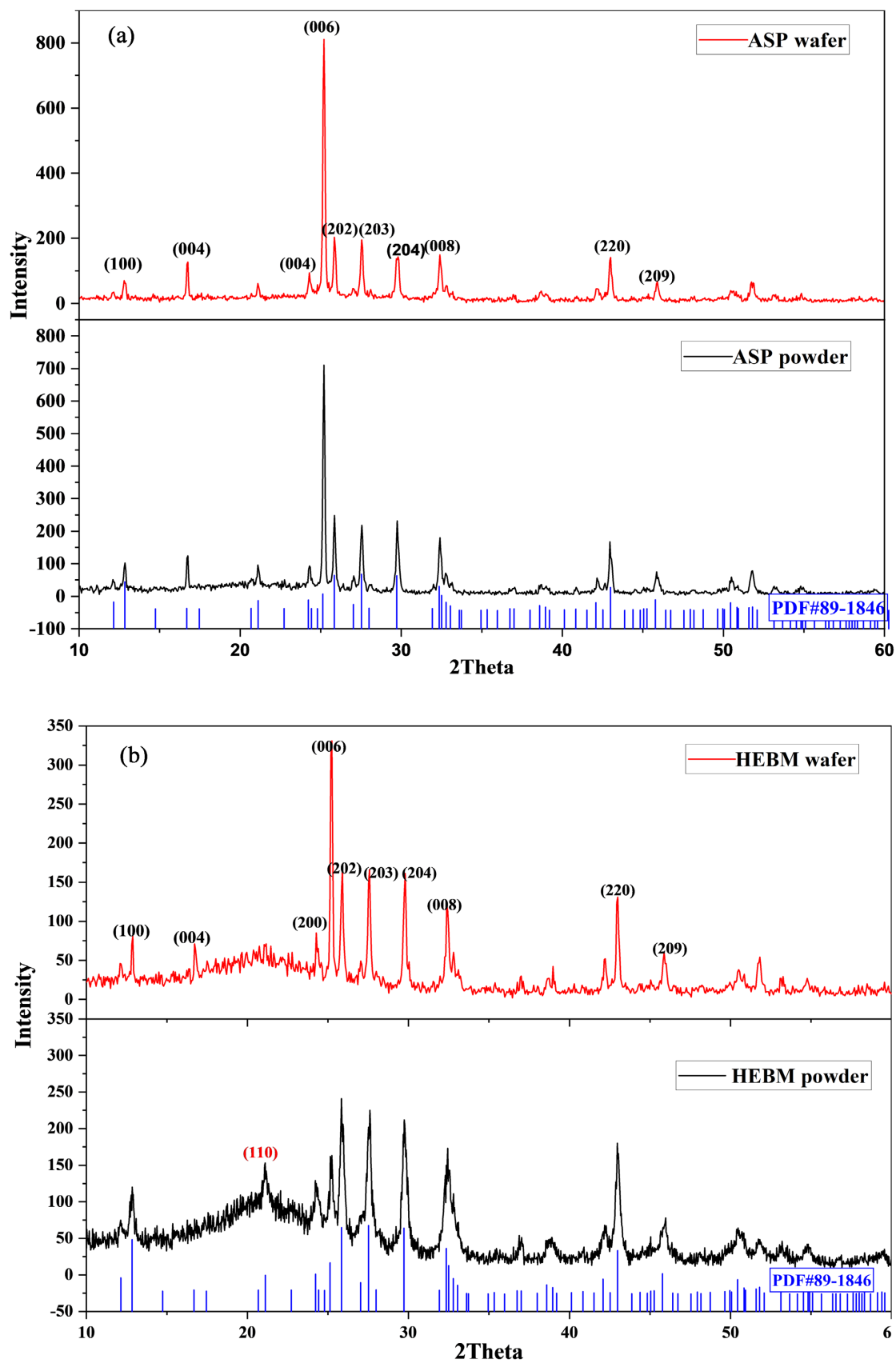


Figure 2. The XRD pattern of $\text{Cs}_3\text{Bi}_2\text{I}_7$: (a) ASP; (b) HEBM.

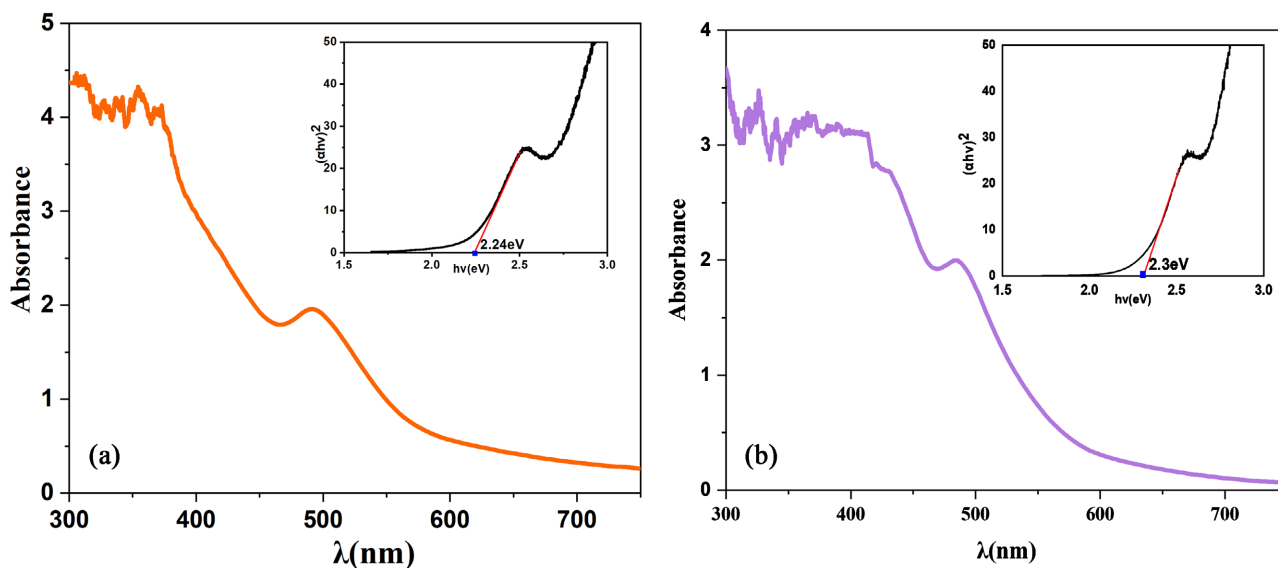


Figure 3. The UV-VIS spectroscopy of two type material.

the experimental feasibility of the method for the synthesis of $\text{Cs}_3\text{Bi}_2\text{I}_9$ polycrystals.

3) TG-DTA

Thermal analysis technology is that when the physical or chemical states of substances change (such as melting, sublimation, dehydration and polymerization, etc.), thermodynamic properties (specific heat, enthalpy and thermal conductivity, etc.) often change, so the physical and chemical change process of substances can be understood by measuring the change of their thermodynamic properties [22]. The thermogram (DTA curve) obtained by DTA is the temperature as the abscissa and the temperature difference between the sample and reference ΔT as the ordinate, and the different endothermic and exothermic peaks show the different thermal transition states of the sample when heated.

The thermal stability of the $\text{Cs}_3\text{Bi}_2\text{I}_9$ is confirmed by thermogravimetric analysis (Figure 4), showing no detectable mass loss until 500°C , confirming good thermal stability of ASP- $\text{Cs}_3\text{Bi}_2\text{I}_9$. As contrast HBEM- $\text{Cs}_3\text{Bi}_2\text{I}_9$ were beginning to decompose at 300°C . It can be clearly seen that the sample prepared by ball milling has decomposition below 400°C , while the polycrystalline powder obtained by anti-solvent method starts to decompose at 500°C and above. Among them, $\text{Cs}_3\text{Bi}_2\text{I}_9$ (Purple curve) prepared by ball milling method does not decompose before 300°C , and it shows three decomposition steps from 100°C to 700°C , corresponding to mass loss of about 70%, 20% and 10% respectively. The temperature of the second step is very close to that of the first step of $\text{Cs}_3\text{Bi}_2\text{I}_9$. The peak value of the first-order differential curve in Figure 4(b) is 370.3°C , the sample in Figure 4(a) corresponds to the sample in Figure 2(a). It can be seen that the crystallization is good, the melting decomposition temperature is relatively higher, and the maximum decomposition rate is 564°C . The whole TAG curve is very consistent with the reported single crystal TAG curve [13].

4) SEM

SEM was used to characterize its micro-structure, in order to observe the properties of powder more directly such as crystallization.

The results obtained from XRD test analysis of the material mentioned above can be explicitly guided. In fact, the crystallization of powder obtained by ASP method is far better than that prepared by HEBM, which is also confirmed by SEM characterization analysis. According to **Figure 5**, it can be clearly observed that ASP powder and HEBM powder have larger crystal particles and better crystallinity under a scanning electron microscope with a magnification of 2000 times at 5 μm .

By observing the cross section and surface flatness of the thin section by SEM (**Figure 6**), it was found that although the surface flatness of sample A was worse than that of sample B, the overall density of the material reflected by the cross section seemed to be stronger than that of A. However, it can be easily seen from the SEM figure of cross section that its crystallinity is much stronger than that of sample B, and its grain size is similar to that of powder SEM, which is much larger than that of sample B.

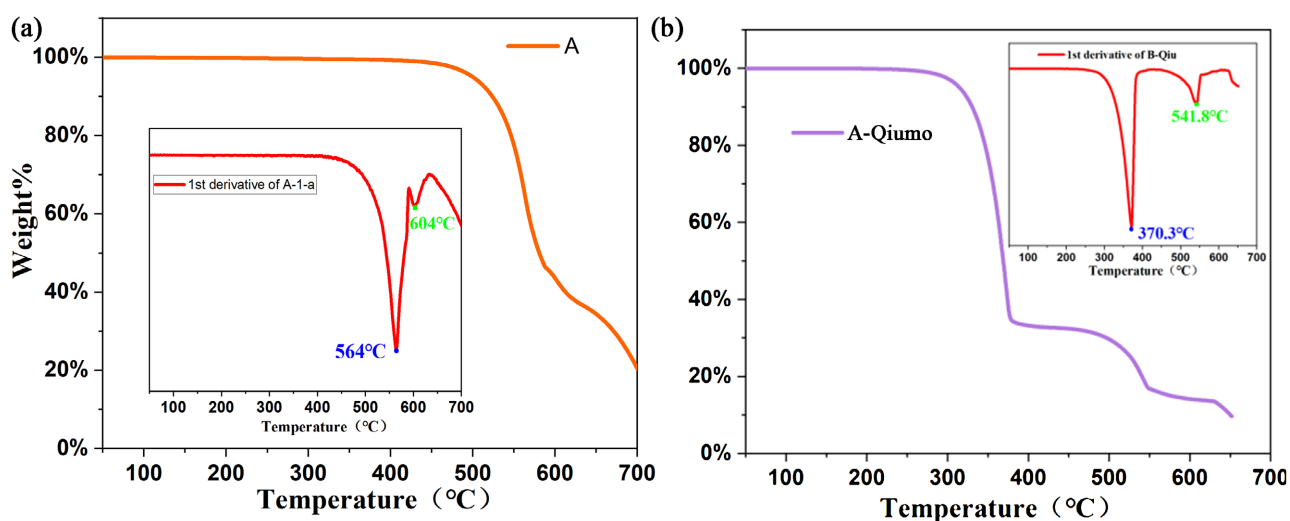


Figure 4. The TAG curve of tow method: (a) ASP; (b) HBEM.

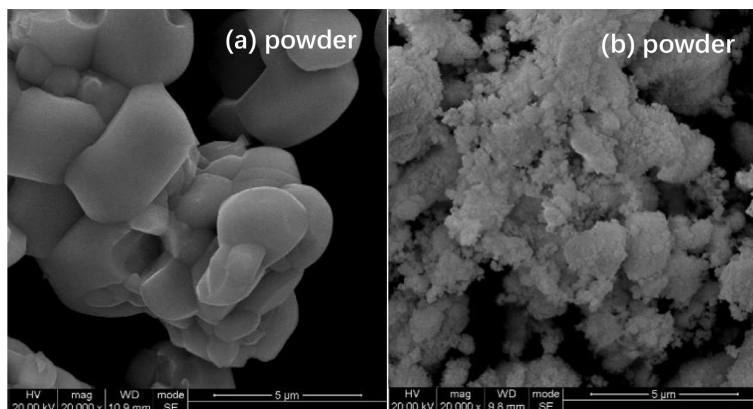


Figure 5. The SEM of powder by two methods.

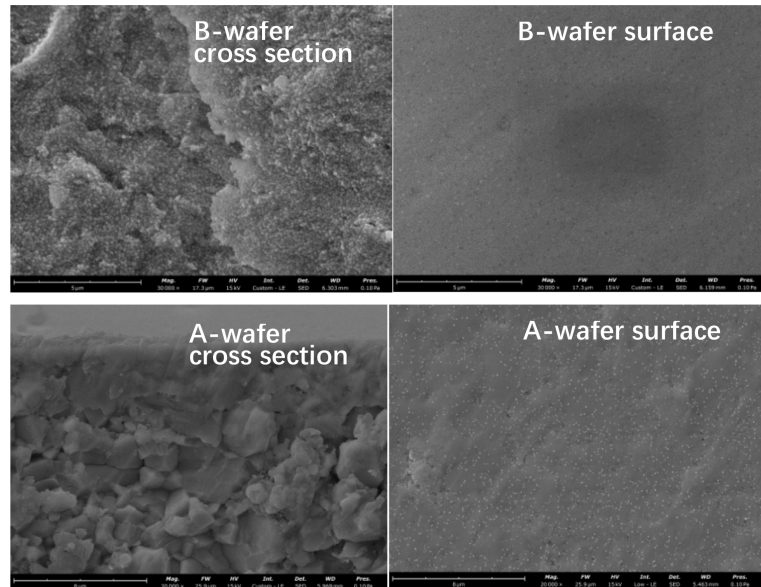


Figure 6. SEM of $\text{Cs}_3\text{Bi}_2\text{I}_9$ wafer's cross-section and surface.

3.2. Device Performance of $\text{Cs}_3\text{Bi}_2\text{I}_9$ Wafer Direct X-Ray Detectors

The performance of devices is affected by many factors, and a lot of useful information has been obtained from the characterization of basic properties of materials. The electrical properties of the materials obtained in the 2 method were characterized. The I - V characteristics and dark current curve were obtained by the semiconductor parameter analyzer, and the dark resistivity and conductivity of the materials were calculated.

As we all know, in semiconductor physics, it is assumed that there are two kinds of carriers, electrons and holes, in semiconductor materials, and the relationship between the current density J and the electric field E can be expressed as [23]

$$J = \sigma E = (nq\mu_n + pq\mu_p)|E| \quad (3-1)$$

where σ represents the conductivity of the material, is the reciprocal of the resistivity, n , p respectively represents the number of electronic holes in the semiconductor, q represents the unit charge, and μ_n , μ_p represents the mobility of electrons and holes. According to Equation (4-1), the conductivity of the material can be obtained by taking the derivative of J with respect to E , in unit of $\Omega^{-1}\cdot\text{cm}^{-1}$.

As **Figure 7(a)** shows, in the electric field intensity range of -30 Vmm^{-1} to 30 Vmm^{-1} , the current density J and the electric field intensity E show a linear relationship, and the ASP- $\text{Cs}_3\text{Bi}_2\text{I}_9$ poly-crystalline wafer shows a smaller current density under the same electric field intensity, that is to say, the resistance value of the sample is greater than that of the HEBM- $\text{Cs}_3\text{Bi}_2\text{I}_9$ sample. The conductivity of the photosensitive element prepared by the two methods is $1.95 \times 10^{-10} \Omega^{-1}\cdot\text{cm}^{-1}$ and $4.53 \times 10^{-11} \Omega^{-1}\cdot\text{cm}^{-1}$, respectively.

The test data is not stable enough when the bias voltage is just added to both

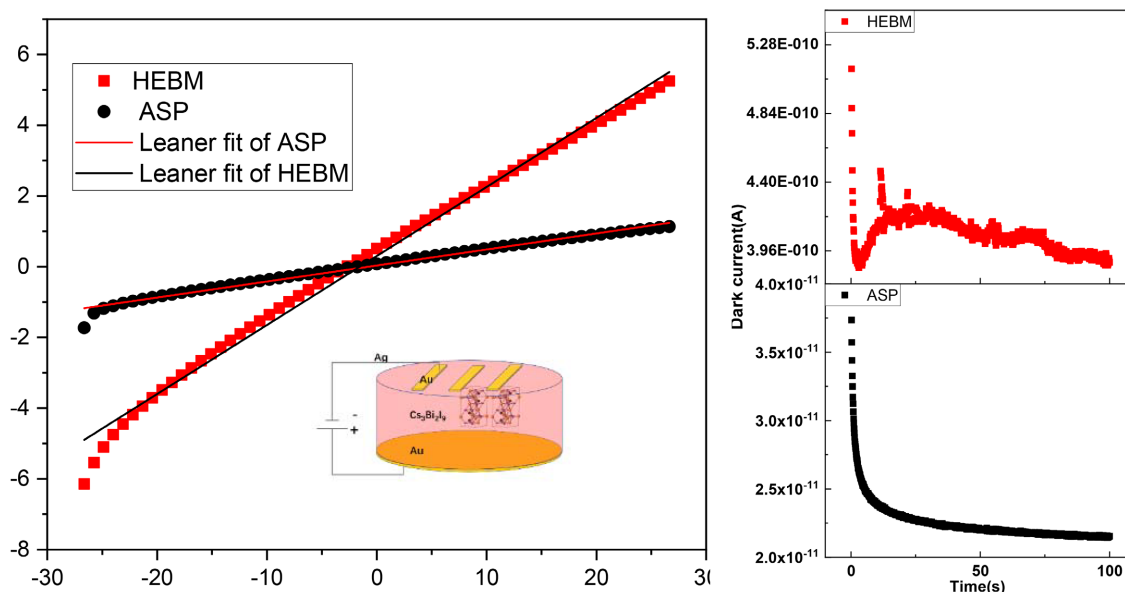


Figure 7. (a) The dark current of ASP-Cs₃Bi₂I₉ wafer and HEBM Cs₃Bi₂I₉ wafer; (b) Dark at different electric field intensities.

ends of the device, so the analysis of dark conductance data starts from 20 s. **Figure 7(b)** shows the devices prepared by two methods. When the applied voltage is 15V, the mean dark current of ASP-Cs₃Bi₂I₉ is about 2.01×10^{-11} A, while the dark current of HEBM-Cs₃Bi₂I₉ is about 4.1×10^{-10} A, which also shows that the former has higher resistivity.

As illustrated in **Figure 8(a)**, compared with Cs₂AgBiBr₆, CdTe, MA₃Bi₂I₉, MAPbI₃, Cs₃Bi₂I₉ exhibited higher absorption coefficient, especially for X-ray photons of 36 - 90 keV, which indicates its potential in medical radiography X-ray detection. As for **Figure 8(b)**, it shows the absorption coefficient corresponding to different materials mentioned above. **Figure 8(c)** shows the relationship between absorption coefficient of Cs₃Bi₂I₉ material and material thickness, in this way, the absorption efficiency of the sheet material at its current thickness can be easily calculated. The two wafer thicknesses obtained in this work are 589 nm and 535 nm respectively; this means an X-ray absorption efficiency of 100% for 35 KeV. The absorption coefficient datum comes from the NIST database [24].

Sensitivity is a key parameter to characterize the detection efficiency of photodetector. The detection sensitivity S_x of X-ray detector is defined as [25]:

$$S_x = \frac{Q}{AX} \quad (3-2)$$

where, A represents the effective irradiation area, in cm²; X represents radiation dose, in unit of Gy; Q is the effective net charge collected by the detector material under X-ray irradiation, which can be expressed as [26]:

$$Q = \int \bar{I}_{\text{photo}}(t) dt \quad (3-3)$$

where, \bar{I}_{photo} represents the average photocurrent, and t represents the effective sampling

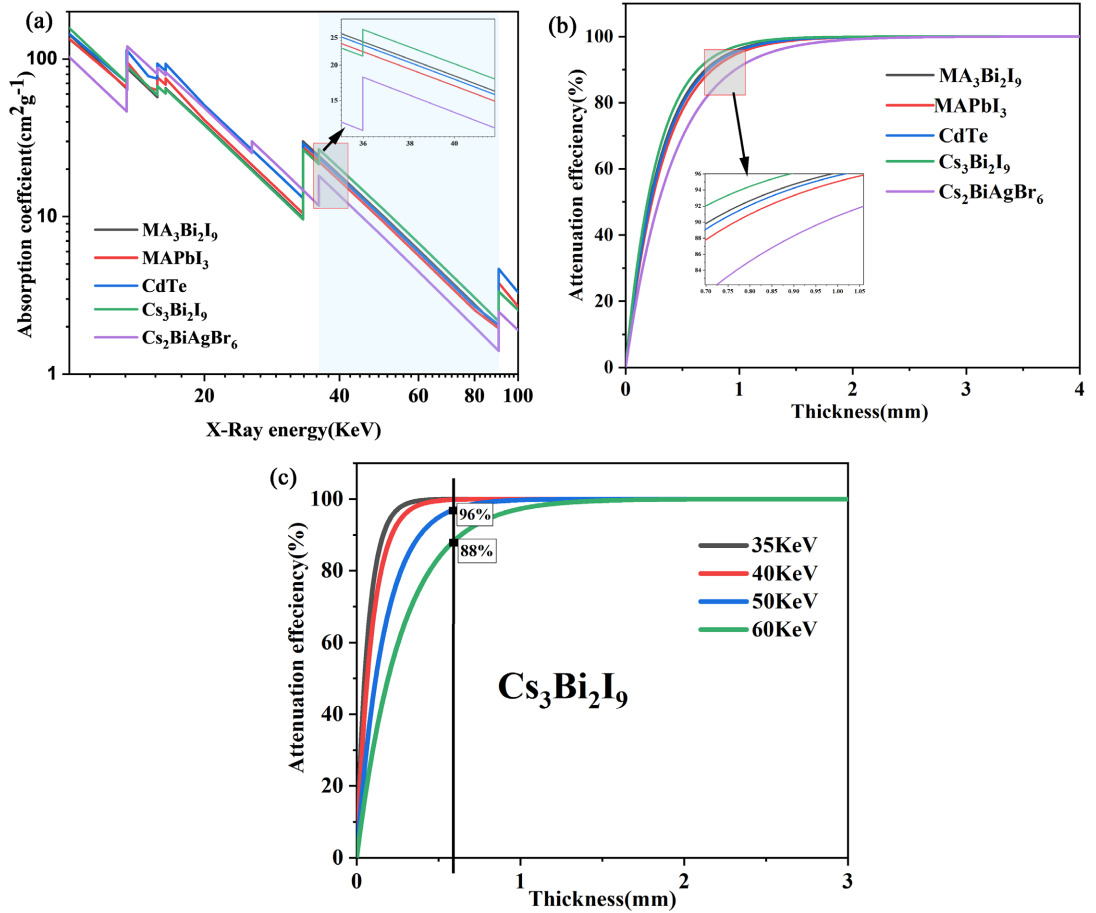


Figure 8. (a) Spectrum of the relationship between absorption coefficient and photon intensity of different materials; (b) The absorption coefficient corresponding to different materials; (c) The relationship between absorption coefficient and material thickness.

time of the detector; According to Equations (3-2) and (3-3), the sensitivity of the detector can be obtained.

The ratio of detector effective signal to noise signal is signal-to-noise ratio (SNR), which is one another of the key parameters to evaluate the overall performance of detector [27]. SNR for X-ray imaging devices is expressed as the ratio of device signal current to noise current, namely [20]:

$$SNR = \frac{I_{\text{signal}}}{I_{\text{noise}}} \tag{3-4}$$

$$I_{\text{signal}} = \bar{I}_{\text{photo}} - \bar{I}_{\text{dark}} \tag{3-5}$$

$$I_{\text{noise}} = \sqrt{\frac{1}{N} \sum_i^N (I_i - \bar{I}_{\text{photo}})^2} \tag{3-6}$$

where I_{signal} is the optical gain, that is, the mean difference between photocurrent and dark current, \bar{I}_{dark} represents the average dark current, \bar{I}_{photo} represents the average photocurrent, and I_{noise} is the standard deviation of the photocurrent of the detector.

As shown in **Figure 9**, different radiation dose rates (7.6 μGyS⁻¹ - 396 μGyS⁻¹)

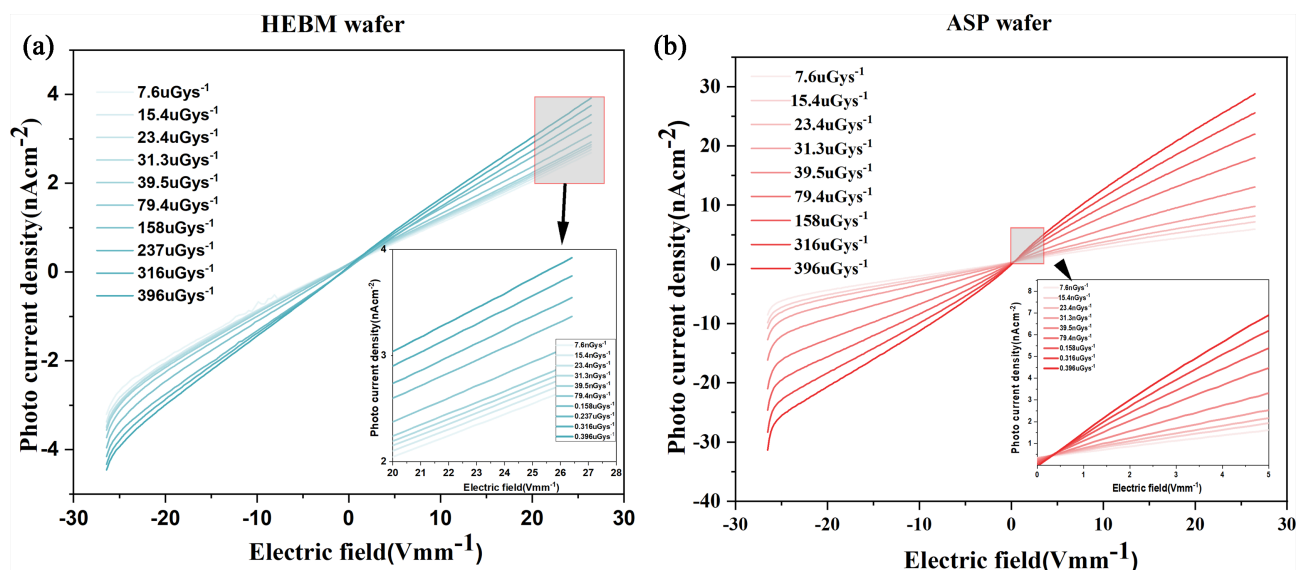


Figure 9. J - E curves at different dose rates. (a) ASP- $\text{Cs}_3\text{Bi}_2\text{I}_9$; (b) HEBM $\text{Cs}_3\text{Bi}_2\text{I}_9$.

were measured respectively. The J - E curve of the detector was obtained by the preparation of polycrystalline powder by HEBM and ASP, and the optical gain of the device was visualized under different irradiation intensities. The slope of the J - E curve, in general, and the device linearity are both good, contrast in the section on the dark conductivity, two kinds of method, the resistivity of ASP sample is greater than HEBM sample material, and the former under X-ray irradiation of photocurrent density larger instead, which further confirmed the samples prepared by the solvent method for better crystallization properties, thus gain more light. The density of J - E curve can directly reflect the size of gain. The denser (blue curves) means the increase of the same irradiation measure, the smaller the optical gain is, and vice versa (red curves).

Figure 10(a) shows the device response diagram prepared by the two methods at 2 s irradiation switch, 15 V bias voltage and 315.5 μGyS^{-1} dose rate. It can be clearly seen that the response signal current of black curve (ASP) is greater than that of red curve (HEBM), while the photocurrent of the latter shows a very obvious noise signal (curve burr). Combined with the performance characterization of materials prepared by the two methods described above, the reason for the poor response performance of HEBM- $\text{Cs}_3\text{Bi}_2\text{I}_9$ detector is still that the crystallization performance of core layer material is lower, and the probability of recombination of carriers in the material body is higher, showing stronger noise signal. **Figure 10(b)** and **Figure 10(c)** show that under the same test bias light measured by conductivity with the increase of irradiation dose rate increased significantly, consistent with the J - E Bright field test results, photocurrent increased with the increase of irradiation dose rate ladder type at the same time also presents the ladder type growth obviously, and irradiation dose rate according to the linear increase response between current linear fitting are also presents linear basically. The response linearity of the device is high.

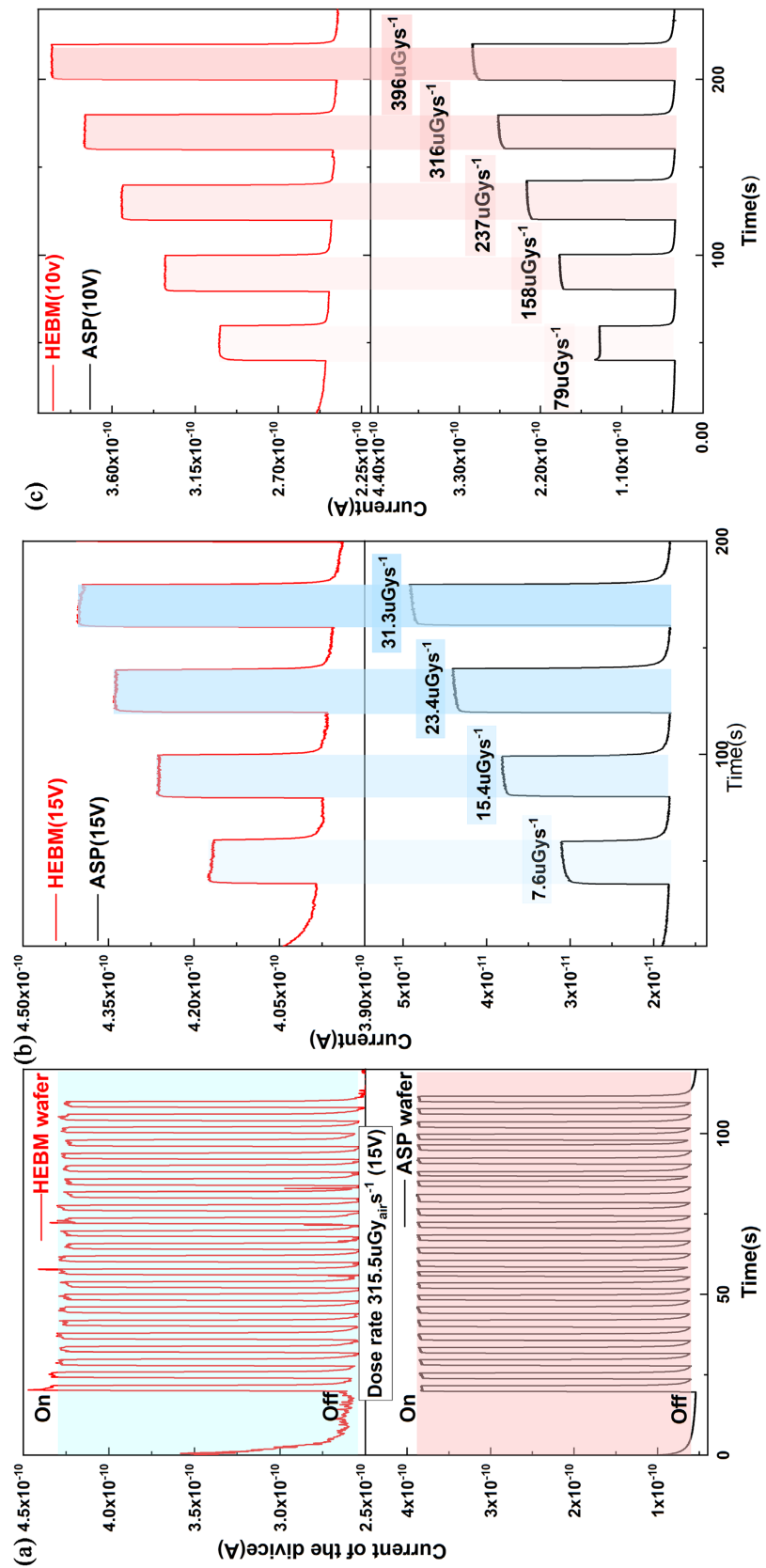


Figure 10. The response characteristics of 2 type $\text{Cs}_3\text{Bi}_2\text{I}_9$ detectors under X-ray radiation. (a) 2 s on-off; (b) dose-rate: $7.6 \mu\text{Gys}^{-1}$ - $31.3 \mu\text{Gys}^{-1}$; (c) dose-rate: $79 \mu\text{Gys}^{-1}$ - $396 \mu\text{Gys}^{-1}$.

Table 1. Important factors have been reported and compared with this work.

Material	Sensitivity ($\mu\text{C}\cdot\text{Gy}_{\text{air}}\cdot\text{s}^{-1}$)	LoD ($\text{nGy}_{\text{air}}\cdot\text{s}^{-1}$)	Electric field(Vmm^{-1})	SNR	type	Ref.
$\text{Cs}_3\text{Bi}_2\text{I}_9$	588	76	28.8	179	Poly-crystal	ASP
$\text{Cs}_3\text{Bi}_2\text{I}_9$	543	155	28.8	65	Poly-crystal	HBEM
$\text{Cs}_3\text{Bi}_2\text{I}_9$	1652	130	50	16.9	Single-crystal	[13]
$\text{Cs}_3\text{Bi}_2\text{I}_9$	111.9	-	45	-	Single-crystal	[14]
$\text{Cs}_3\text{Bi}_2\text{I}_9$	964	44.6	30	66	Single-crystal	[20]
$\text{MA}_3\text{Bi}_2\text{I}_9$	872	31	10	35.6	Single-crystal	[15]
$\alpha\text{-Se}$	440	-	15	-	Amorphous	[28]

4. Conclusions

In this paper, two methods of anti-solvent and ball milling were used to synthesize $\text{Cs}_3\text{Bi}_2\text{I}_9$. In addition, the basic properties of the materials were tested and analyzed, and it was found that ASP method had better crystallinity. Although HBEM's crystallinity was not good enough, it was better than the crystal uniformity, which made the wayer surface smoother and more conducive to obtaining good ohmic contact. The X-ray detector was fabricated by pressing polycrystalline powders obtained from two methods mentioned above.

When testing and analyzing the electrical properties of 2 types of materials, it is found that the resistivity of ASP material is significantly higher than that of HBEM, which is also the reason why the former has lower dark current under the same electric field intensity, which is conducive to signal discrimination of the device. Finally, the response performance was analyzed for 2 devices, and important device parameters including SNR and sensitivity were obtained. In order to more conveniently explain the advantages and disadvantages of this working device, some typical device parameter pairs are selected to report, for example, see **Table 1**.

Conflicts of Interest

The author declares no conflicts of interest regarding the publication of this paper.

References

- [1] Zhou, H., Chen, Q., Li, G., *et al.* (2014) Photovoltaics. Interface Engineering of Highly Efficient Perovskite Solar Cells. *Science*, **345**, 542-546. <https://doi.org/10.1126/science.1254050>
- [2] Green, M.A., Ho-Baillie, A. and Snaith, H.J. (2014) The Emergence of Perovskite Solar Cells. *Nature Photonics*, **8**, 506-514. <https://doi.org/10.1038/nphoton.2014.134>
- [3] Yang, W.S., *et al.* (2017) Iodide Management in Formamidinium-Lead-Halide-Based Perovskite Layers for Efficient Solar Cells. *Science*, **356**, 1376-1379.
- [4] Xu, W., Hu, Q., Bai, S., *et al.* (2019) Rational Molecular Passivation for High-Per-

- formance Perovskite Light-Emitting Diodes. *Nature Photonics*, **13**, 418-424. <https://doi.org/10.1038/s41566-019-0390-x>
- [5] Sakdinawat, A. and Attwood, D. (2009) Nanoscale X-Ray Imaging. *Nature Photonics*, **4**, 840-848. <https://doi.org/10.1038/nphoton.2010.267>
- [6] Chen, Q., Wu, J., Ou, X., *et al.* (2018) All-Inorganic Perovskite Nanocrystal Scintillators. *Nature*, **561**, 88-93. <https://doi.org/10.1038/s41586-018-0451-1>
- [7] Heiss, W. and Brabec, C. (2016) X-Ray Imaging: Perovskites Target X-Ray Detection. *Nature Photonics*, **10**, 288-289. <https://doi.org/10.1038/nphoton.2016.54>
- [8] Yakunin, S., *et al.* (2015) Detection of X-Ray Photons by Solution-Processed Lead Halide Perovskites. *Nature Photonics*, **9**, 444-449. <https://doi.org/10.1038/nphoton.2015.82>
- [9] Kim, Y.C., Kim, K.H., Son, D.Y., *et al.* (2017) Printable Organometallic Perovskite Enables Large-Area, Low-Dose X-Ray Imaging. *Nature*, **550**, 87-91. <https://doi.org/10.1038/nature24032>
- [10] Basiricò, L., Ciavatti, A. and Fraboni, B. (2020) Solution-Grown Organic and Perovskite X-Ray Detectors: A New Paradigm for the Direct Detection of Ionizing Radiation. *Advanced Materials Technologies*, **6**, Article ID: 2000475. <https://doi.org/10.1002/admt.202000475>
- [11] Armaroli, G., Ferlauto, L., Lédée, F., *et al.* (2021) X-Ray-Induced Modification of the Photophysical Properties of MAPbBr₃ Single Crystals. *ACS Applied Materials & Interfaces*, **13**, 58301-58308. <https://doi.org/10.1021/acsami.1c16072>
- [12] He, Y., Hadar, I. and Kanatzidis, M.G. (2021) Detecting Ionizing Radiation Using Halide Perovskite Semiconductors Processed through Solution and Alternative Methods. *Nature Photonics*, **16**, 14-26.
- [13] Zhang, Y., Liu, Y., Xu, Z., *et al.* (2020) Nucleation-Controlled Growth of Superior Lead-Free Perovskite Cs₃Bi₂I₉ Single-Crystals for High-Performance X-Ray Detection. *Nature Communications*, **11**, Article No. 2304. <https://doi.org/10.1038/s41467-020-16034-w>
- [14] Sun, Q., Xu, Y., Zhang, H., *et al.* (2018) Optical and Electronic Anisotropies in Perovskite Crystals of Cs₃Bi₂I₉, Studies of Nuclear Radiation Detection. *Journal of Materials Chemistry A*, **6**, 23388-23395. <https://doi.org/10.1039/C8TA09525F>
- [15] Liu, Y.C., Zhang, Y.X., Zhou, Y., *et al.* (2020) Large Lead-Free Perovskite Single Crystal for High-Performance Coplanar X-Ray Imaging Applications. *Advanced Optical Materials*, **8**, Article ID: 2000814. <https://doi.org/10.1002/adom.202000814>
- [16] Wang, Z., Sun, R., Liu, N., *et al.* (2021) X-Ray Imager of 26-m Resolution Achieved by Perovskite Assembly. *Nano Research*, **15**, 2399-2404. <https://doi.org/10.1007/s12274-021-3808-y>
- [17] Zhang, H., Yang, Z., Zhou, M., *et al.* (2021) Reproducible X-Ray Imaging with a Perovskite Nanocrystal Scintillator Embedded in a Transparent Amorphous Network Structure. *Advanced Materials*, **33**, Article ID: 2102529. <https://doi.org/10.1002/adma.202102529>
- [18] Zheng, J., Zeng, Y., Wang, J., *et al.* (2021) Hydrogen-Rich 2D Halide Perovskite Scintillators for Fast Neutron Radiography. *Journal of the American Chemical Society*, **143**, 21302-21311. <https://doi.org/10.1021/jacs.1c08923>
- [19] Zhang, H., Xu, Y., Sun, Q., *et al.* (2018) Lead Free Halide Perovskite Cs₃Bi₂I₉ Bulk Crystals Grown by a Low Temperature Solution Method. *CrystEngComm*, **20**, 4935-4941. <https://doi.org/10.1039/C8CE00925B>
- [20] Wei, S., Tie, S., Shen, K., *et al.* (2021) High-Performance X-Ray Detector Based on

- Liquid Diffused Separation Induced Cs₃Bi₂I₉ Single Crystal. *Advanced Optical Materials*, **9**, Article ID: 2101351. <https://doi.org/10.1002/adom.202101351>
- [21] Kawai, T. and Shimanuki, S. (1993) Optical Studies of (CH₃NH₃)₃Bi₂I₉ Single Crystals. *Physica Status Solidi (b)*, **177**, K43-K45. <https://doi.org/10.1002/pssb.2221770128>
- [22] Pagoria, P.F., Lee, G.S., Mitchell, A.R., *et al.* (2002) A Review of Energetic Materials Synthesis. *Thermochimica Acta*, **384**, 187-204. [https://doi.org/10.1016/S0040-6031\(01\)00805-X](https://doi.org/10.1016/S0040-6031(01)00805-X)
- [23] Dobson, P.J. (1982) Physics of Semiconductor Devices (2nd edn). *Physics Bulletin*, **33**, 139. <https://doi.org/10.1088/0031-9112/33/4/035>
- [24] Berger, M.J., Hubbell, J.H., Seltzer, S.M., *et al.* (2013) XCOM: Photon Cross Sections Database: NIST Standard Reference Database 8. NIST. <https://www.nist.gov/pml/xcom-photon-cross-sections-database>
- [25] Zhu, X.H., Zhao, B.J., Zhu, S.F., *et al.* (2007) Growth of PbI₂ Crystal with Excessive Pb and Its Characterization. *Journal of Semiconductors*, **28**, 898.
- [26] Sun, H., Zhu, X.H., Yang, D.Y., Yang, J., Gao, X.Y. and Li, X. (2014) Morphological and Structural Evolution during Thermally Physical Vapor Phase Growth of PbI₂ Polycrystalline Thin Films. *Journal of Crystal Growth*, **29**, 34. <https://doi.org/10.1016/j.jcrysgro.2014.07.043>
- [27] Liu, Y., Zhang, Y.X., Zhu, X., *et al.* (2021) Triple-Cation and Mixed-Halide Perovskite Single Crystal for High-Performance X-Ray Imaging. *Advanced Materials*, **33**, Article ID: 2006010. <https://doi.org/10.1002/adma.202006010>
- [28] Polischuk, B.T., Rougeot, H., Wong, K., *et al.* (1999) Direct Conversion Detector for Digital Mammography. *Proceedings of SPIE—The International Society for Optical Engineering*, **3659**, 417-425.